chemosensors

MDPI

Article

Benzoxazole Iminocoumarins as Multifunctional Heterocycles with Optical pH-Sensing and Biological Properties: Experimental, Spectroscopic and Computational Analysis

Marina Galić [1], Ana Čikoš [2], Leentje Persoons [3], Dirk Daelemans [3], Karolina Vrandečić [4], Maja Karnaš [4], Marijana Hranjec [1,*] and Robert Vianello [5,*]

[1] Department of Organic Chemistry, Faculty of Chemical Engineering and Technology, University of Zagreb, 10000 Zagreb, Croatia; mgalic@fkit.unizg.hr
[2] NMR Centre, Ruđer Bošković Institute, 10000 Zagreb, Croatia; ana.cikos@irb.hr
[3] Molecular Genetics and Therapeutics in Virology and Oncology Research Group, KU Leuven Department of Microbiology, Immunology and Transplantation, Rega Institute, B-3000 Leuven, Belgium; leentje.persoons@kuleuven.be (L.P.); dirk.daelemans@kuleuven.be (D.D.)
[4] Faculty of Agrobiotechnical Sciences Osijek, Josip Juraj Strossmayer University of Osijek, 31000 Osijek, Croatia; karolina.vrandecic@fazos.hr (K.V.); mkarnas@fazos.hr (M.K.)
[5] Laboratory for the Computational Design and Synthesis of Functional Materials, Division of Organic Chemistry and Biochemistry, Ruđer Bošković Institute, 10000 Zagreb, Croatia
* Correspondence: mhranjec@fkit.unizg.hr (M.H.); robert.vianello@irb.hr (R.V.)

Abstract

A novel series of benzoxazole-derived iminocoumarins was synthesized via a Knoevenagel condensation and fully characterized using NMR, UV–Vis spectroscopy, and computational methods. Their photophysical properties were systematically examined in solvents of varying polarity, revealing pronounced effects of both substituents and solvent environment on absorption maxima and intensity. Derivatives bearing electron-donating substituents on the coumarin core exhibited distinct and reversible pH-responsive spectral shifts, confirming their potential as optical pH probes. Experimental pK_a values derived from absorption titrations showed excellent agreement with DFT-calculated data, validating the proposed protonation-deprotonation equilibria and associated electronic structure changes. Structure–property relationships revealed that electron-donating groups enhance intramolecular charge transfer, while electron-withdrawing substituents modulate spectral response and stability. In parallel, the compounds were evaluated for antiproliferative, antiviral, and antifungal activities in vitro. Strong electron-donating substituents were associated with potent but non-selective cytotoxicity, whereas derivatives bearing electron-withdrawing groups displayed moderate and more selective antiproliferative effects against leukemia cell lines. Antifungal screening revealed moderate inhibition of phytopathogenic fungi, particularly for compounds with electron-withdrawing or methoxy substituents. Overall, these findings demonstrate that benzoxazole iminocoumarins represent a promising class of multifunctional heterocycles with potential applications as optical pH sensors and scaffolds for bioactive compound development.

Keywords: iminocoumarins; benzoxazole derivatives; optical pH sensors; solvent effects; DFT calculations; spectroscopic characterization; antiproliferative activity; antifungal activity

Received: 1 December 2025
Revised: 23 December 2025
Accepted: 31 December 2025
Published: 3 January 2026

1. Introduction

Heterocyclic molecules are indispensable scaffolds in medicinal and pharmaceutical chemistry, with great potential as biologically active agents [1,2]. In addition, they exhibit

https://doi.org/10.3390/chemosensors14010015

diverse spectral features and optical properties [3], making them one of the most extensively studied classes of organic compounds with wide-ranging applications. The design and development of small molecules for (chemo)sensing continues to be an area of significant interest in organic chemistry and sensing technology [4–6].

Coumarin derivatives, particularly hydroxy- and iminocoumarins, have long been recognized for their pH-dependent optical properties and sensing capabilities, as demonstrated in pioneering studies by Wolfbeis and co-workers [7,8]. Building on this foundation, more recent efforts have focused on extending conjugation and introducing heterocyclic acceptor groups to tune charge-transfer behavior and spectral response. In this context, the iminocoumarin moiety represents a multifunctional unit and an important building block in D-π-A systems, enabling applications in optoelectronics and pH sensing [9]. In parallel, a variety of novel coumarin-based fluorescent pH indicators have been developed, exploiting protonation-induced modulation of intramolecular charge transfer to achieve pronounced absorption and emission changes across biologically relevant pH ranges [10]. In particular, heterocycle-fused and benzocoumarin-type systems have attracted attention as ratiometric and environment-sensitive probes, demonstrating that incorporation of additional aromatic or heteroaromatic units can significantly enhance pH sensitivity and spectral tunability [11].

The photophysical behavior of coumarin derivatives is strongly governed by substituent effects within a D-π-A framework [12–14]. In particular, electron-donating groups at the 7-position of the coumarin core increase electron density on the aromatic system and raise the HOMO energy level, while electron-accepting substituents at the 3-position stabilize the LUMO [15,16]. This spatial separation of donor and acceptor functionalities enhances intramolecular charge transfer upon π–π excitation, typically resulting in bathochromic shifts and increased absorption intensity. The magnitude of these effects depends on the electronic strength of the substituents and their conjugative coupling with the coumarin π-system, providing a well-established strategy for tuning spectral response and pH sensitivity in coumarin-based chromophores. Extension of the π-electronic conjugation, as demonstrated in several benzazole-derived coumarins, further modulates the photophysical properties [15–19]. Notably, coumarin–benzoxazole hybrid chromophores have been reported to exhibit strong electronic coupling between donor and acceptor subunits, leading to enhanced intramolecular charge transfer and pronounced solvatochromic and fluorescence responses [20]. Although these systems have been primarily investigated in the context of photophysical and nonlinear optical properties, their structural features and tunable emission behavior render them highly attractive platforms for the development of optical pH sensors. Iminocoumarins have been reported as functional and optical materials [21], fluorescent brighteners [22], laser dyes [23], solar energy collectors [24], pigments, probes for physiological measurements [25], and fluorescent labels [26]. In this context, benzoxazole derivatives themselves have been shown to display pH-dependent fluorescence responses arising from protonation–deprotonation equilibria and excited-state intramolecular proton transfer processes, further underscoring the suitability of benzoxazole-containing frameworks for optical sensing applications [27].

We recently reported the spectroscopic characterization of benzimidazole- and imidazo [4,5-*b*]pyridine-derived iminocoumarins as potential pH-sensing molecules (Figure 1) [17,28]. These findings are consistent with earlier reports on coumarin- and benzazole-based fluorescent pH probes, which highlight the importance of heterocyclic acceptor units and conjugation length in governing proton-responsive optical behavior [10,11,20,27]. Solvent polarity and the electronic nature of substituents and heteroatoms on the benzazole cores were found to significantly influence their spectral responses. These results were further supported by computational analysis, showing excellent agreement between experimental and calculated pK_a values and electronic excitations.

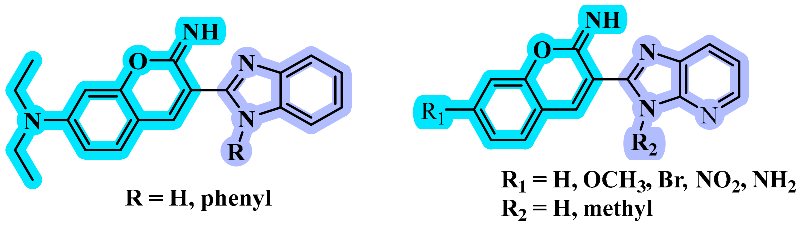

Figure 1. Previously synthesized benzazole-derived iminocoumarins (see refs. [17] and [28]).

Building on these findings, and given the promise of benzazoles as key subunits in the design of D-π-A system-based materials with potential applications in biomedical sciences and optical probing, we synthesized several iminocoumarin-derived benzoxazoles bearing various substituents on the coumarin core. The introduced substituents were selected to enable a systematic evaluation of structure–property relationships. Electron-donating groups (e.g., hydroxy and dialkylamino substituents) were employed to enhance intramolecular charge transfer and to promote pH-responsive optical behavior, whereas electron-withdrawing substituents (e.g., nitro and halogen groups) were included to modulate electronic density, conjugation, and stability. In addition, substituents with different steric demands were chosen to assess their influence on molecular planarity, spectroscopic response, and biological activity. This design strategy allows direct correlation between substituent effects and the observed photophysical, acid–base, and biological properties.

Despite substantial progress in the development of coumarin- and benzazole-based fluorescent systems, benzoxazole–iminocoumarin hybrids remain largely unexplored, particularly with regard to a unified assessment of their pH-responsive optical properties, electronic structure, and biological activity. Moreover, detailed correlations between substituent-induced electronic effects, protonation equilibria, and spectroscopic response, supported by computational analysis, are still lacking. To address this gap, the spectroscopic features of the present iminocoumarin-derived benzoxazoles were investigated in solvents of different polarity, together with their acid–base properties, to evaluate their potential as optical pH indicators. The experimental findings were complemented by detailed computational studies, and, in view of the broad spectrum of biological activities reported for iminocoumarin derivatives [29,30], the antiproliferative, antiviral, and antifungal activities of the new compounds were also evaluated in vitro.

2. Experimental Part

2.1. Chemistry

2.1.1. General Methods

All chemicals and solvents were obtained from commercial suppliers (Aldrich, Acros, Fluka). Melting points were measured on an SMP11 Bibby apparatus and are uncorrected. NMR spectra were recorded in DMSO-d_6 using TMS as an internal standard on Bruker AV300, Avance III HD 400, or AV600 spectrometers (^{1}H: 300–600 MHz; ^{13}C: up to 151 MHz), with chemical shifts reported in ppm (δ). Reaction progress and compound purity were monitored by TLC on Merck silica gel 60 F254 plates under UV light (254 or 366 nm). Column chromatography was performed on silica gel (0.063–0.200 mm, Fluka), and flash chromatography using an Interchim puriFlash XS520 Plus system. Microwave-assisted reactions were carried out in a Milestone Start S microwave oven using quartz cuvettes (up to 40 bar), while parallel synthesis was conducted using a Radleys Carousel 12 Plus Reaction Station.

Synthesis of compound **2**

Compound **2** was prepared from **1** (4.00 g, 60.55 mmol), trimethylsilyl chloride (7.69 mL, 60.55 mmol), and ethanol (7.07 mL, 121.1 mmol) at 0 °C for 17 h. After filtration, white crystals were obtained (5.17 g, 58%) and washed with dry diethyl ether. Owing to their air sensitivity, the product was used immediately in subsequent cyclization reactions of the 2-cyanomethyl precursor [31].

Synthesis of compound **4**

Compound **4** was prepared from **2** (0.75 g, 5.05 mmol) and **3** (0.37 g, 3.36 mmol) by microwave irradiation at 120 °C for 1 h (500 W, 40 bar) in methanol. After cooling to room temperature, the crude product was purified by flash chromatography (CH_2Cl_2/MeOH, 100:1) to afford white crystals (0.51 g, 96%); m.p. 72–73 °C. ^{1}H NMR (600 MHz, DMSO-d_6) δ 7.79–7.75 (m, 2H, H_{arom}), 7.46–7.40 (m, 2H, H_{arom}), 4.70 (s, 2H, CH_2); ^{13}C NMR (151 MHz, DMSO-d_6) δ 158.13, 151.01, 140.83, 126.13, 125.39, 120.25, 115.59, 111.38, 18.88.

2.1.2. General Method for Preparation of Compounds **11–16**

A solution of equimolar amounts of 2-cyanomethylbenzoxazole **4**, corresponding heteroaromatic aldehydes **5–10**, and a few drops of piperidine in absolute ethanol (2 mL) was refluxed for 3 h [18,32]. After the reaction mixture was cooled to room temperature, the crude product was purified by column chromatography using dichloromethane/methanol (100:1) as eluent.

3-(benzo[*d*]oxazol-2-yl)-2*H*-chromen-2-imine **11**

Compound **11** was prepared using the described method from **4** (0.100 g, 0.63 mmol) and **5** (0.066 mL, 0.632 mmol) in absolute ethanol (2 mL) to obtain **11** as orange powder 0.132 g (79%); m.p. 162–163 °C; ^{1}H NMR (600 MHz, DMSO) (δ/ppm): 9.09 (s, 1H, H_{arom}), 8.01 (dd, J_1 = 7.80 Hz, J_2 = 1.62 Hz, 1H, H_{arom}), 7.88–7.86 (m, 1H, H_{arom}), 7.84–7.82 (m, 1H, H_{arom}), 7.79–7.56 (m, 1H, H_{arom}), 7.52–7.48 (m, 2H, H_{arom}), 7.48–7.45 (m, 2H, H_{arom}); ^{13}C NMR (151 MHz, DMSO) (δ/ppm): 158.85, 156.41, 154.57, 150.50, 146.79, 141.56, 134.63, 130.51, 126.63, 125.59, 125.49, 120.56, 118.83, 116.70, 114.80, 111.46; Elemental analysis: Found: C, 73.3; H, 4.2; N, 10.6; O, 12.3%; molecular formula $C_{16}H_{10}N_2O_2$ requires: C, 73.1; H, 4.0; N, 10.8; O, 12.1%; MS (ESI): m/z = 264.11 ([M + 2]$^+$).

3-(benzo[*d*]oxazol-2-yl)-2-imino-2*H*-chromen-7-ol **12**

Compound **12** was prepared using the described method from **4** (0.100 g, 0.63 mmol) and **6** (0.087 g, 0.632 mmol) in absolute ethanol (2 mL) to obtain **12** as yellow powder 0.076 g (43%); m.p. > 230 °C; ^{1}H NMR (600 MHz, DMSO) (δ/ppm): 8.96 (s, 1H, H_{arom}), 7.83 (d, J = 8.58 Hz, 1H, H_{arom}), 7.82–7.78 (m, 2H, H_{arom}), 7.47–7.41 (m, 2H, H_{arom}), 6.89 (dd, J_1 = 8.55 Hz, J_2 = 2.31 Hz, 1H, H_{arom}), 6.81 (d, J = 2.16 Hz, 1H, H_{arom}); ^{13}C NMR (151 MHz, DMSO) (δ/ppm): 164.28, 159.55, 157.00, 156.84, 150.41, 147.13, 141.69, 132.23, 126.11, 125.39, 120.21, 114.66, 111.48, 111.27, 109.56, 102.43; Elemental analysis: Found: C, 69.1; H, 4.0; N, 10.1; O, 17.3%; molecular formula $C_{16}H_{10}N_2O_3$ requires: C, 68.8; H, 3.8; N, 9.8; O, 17.5%; MS (ESI): m/z = 279.98 ([M + 1]$^+$).

3-(benzo[*d*]oxazol-2-yl)-*N*,*N*-diethyl-2-imino-2*H*-chromen-7-amine **13** [30]

Compound **13** was prepared using the described method from **4** (0.100 g, 0.63 mmol) and **7** (0.122 g, 0.632 mmol) in absolute ethanol (2 mL) to obtain **13** as orange powder 0.135 g (64%); m.p. 164–165 °C;^{1}H NMR (600 MHz, DMSO) (δ/ppm): δ 8.81 (s, 1H, H_{arom}), 7.77–7.73 (m, 2H, H_{arom}), 7.70 (d, J = 9.00 Hz, 1H, H_{arom}), 7.41–7.39 (m, 2H, H_{arom}), 6.82 (dd, J_1 = 8.97 Hz, J_2 = 2.43 Hz, 1H, H_{arom}), 6.62 (d, J = 2.34 Hz, 1H, Hz, H_{arom}), 3.51 (q, J = 7.08 Hz, 4H, CH_2), 1.16 (t, J = 7.05 Hz, 6H, CH_3); ^{13}C NMR (151 MHz, DMSO) (δ/ppm): 160.40, 157.90, 157.39, 152.95, 150.35, 146.64, 141.92, 131.84, 125.55, 125.18, 119.80, 111.04, 110.43, 108.11, 105.24, 96.55, 44.86 (2C), 12.83 (2); Elemental analysis: Found: C, 72.1; H, 6.1; N, 12.2; O, 9.8%; molecular formula $C_{20}H_{19}N_3O_2$ requires: C, 72.3; H, 5.8; N, 12.4; O, 9.5%; MS (ESI): m/z = 335.07 ([M + 2]$^+$).

3-(benzo[*d*]oxazol-2-yl)-7-methoxy-2*H*-chromen-2-imine **14**

Compound **14** was analogously prepared from **4** (0.100 g, 0.63 mmol) and **8** (0.096 g, 0.632 mmol) in absolute ethanol (2 mL) to obtain **14** as orange crystals 0.114 g (61%); m.p. 164–165 °C; ^{1}H NMR (600 MHz, DMSO) (δ/ppm): 9.00 (s, 1H, H$_{arom}$), 7.92 (d, J = 8.70 Hz, 1H, H$_{arom}$), 7.83 (dd, J_1 = 7.44 Hz, J_2 = 1.77 Hz, 1H, H$_{arom}$), 7.79 (dd, J_1 = 8.16 Hz, J_2 = 1.08 Hz, 1H, H$_{arom}$), 7.47–7.42 (m, 2H, H$_{arom}$), 7.10 (d, J = 2.40 Hz, 1H, H$_{arom}$), 7.06 (dd, J_1 = 8.64 Hz, J_2 = 2.40 Hz, 1H, H$_{arom}$); ^{13}C NMR (151 MHz, DMSO) (δ/ppm): 164.96, 159.32, 156.88, 156.69, 150.45, 146.90, 141.66, 131.78, 126.25, 125.44, 120.30, 113.92, 112.50, 111.31, 110.76, 100.92, 56.75; Elemental analysis: Found: C, 70.0; H, 4.1; N, 9.2; O, 16.9%; molecular formula $C_{17}H_{12}N_2O_3$ requires: C, 69.7; H, 4.3; N, 9.4; O, 16.6%; MS (ESI): m/z = 294.08 ([M + 2]$^+$).

3-(benzo[*d*]oxazol-2-yl)-6-nitro-2*H*-chromen-2-imine **15**

Compound **15** was analogously prepared from **4** (0.100 g, 0.63 mmol) and **9** (0.106 g, 0.632 mmol) in absolute ethanol (2 mL) to obtain **15** as orange powder 0.100 g (51%); m.p. 205–206 °C; ^{1}H NMR (600 MHz, DMSO) (δ/ppm): 9.24 (s, 1H, H$_{arom}$), 8.99 (d, J = 2.76 Hz, 1H, H$_{arom}$), 8.52 (dd, J_1 = 9.06, J_2 = 2.70 Hz, 1H, H$_{arom}$), 7.89 (dd, J_1 = 7.74, J_2 = 1.50 Hz, 1H, H$_{arom}$), 7.85 (d, J = 8.04 Hz, 1H, H$_{arom}$), 7.72 (d, J = 9.12 Hz, 1H, H$_{arom}$), 7.52 (td, J_1 = 7.68, J_2 = 1.38 Hz, 1H, H$_{arom}$), 7.47 (td, J_1 = 7.59, J_2 = 1.18 Hz, 1H, H$_{arom}$). ^{13}C NMR (151 MHz, DMSO) (δ/ppm): 158.20, 158.04, 155.46, 150.53, 145.39, 144.32, 141.48, 128.64, 126.99, 126.18, 125.76, 120.77, 119.20, 118.27, 116.71, 111.56; Elemental analysis: Found: C, 62.5; H, 3.3; N, 13.2; O, 21.0%; molecular formula $C_{16}H_9N_3O_4$ requires: C, 62.7; H, 3.1; N, 13.5; O, 20.7%; MS (ESI): m/z = 309.31 ([M + 2]$^+$).

3-(benzo[*d*]oxazol-2-yl)-6-bromo-2*H*-chromen-2-imine **16**

Compound **16** was analogously prepared from **4** (0.100 g, 0.63 mmol) and **10** (0.127 g, 0.632 mmol) in absolute ethanol (2 mL) to obtain **16** as light yellow powder 0.125 g (65%); m.p. 193–194 °C; ^{1}H NMR (600 MHz, DMSO) (δ/ppm): 9.03 (s, 1H, H$_{arom}$), 8.26 (d, J = 2.40 Hz, 1H, H$_{arom}$), 7.90 (dd, J_1 = 8.79, J_2 = 2.43 Hz, 1H, H$_{arom}$), 7.87 (dd, J_1 = 7.71, J_2 = 1.35 Hz, 1H, H$_{arom}$), 7.84 (dd, J_1 = 7.77, J_2 = 1.17 Hz, 1H, H$_{arom}$), 7.52–7.45 (m, 3H, H$_{arom}$). ^{13}C NMR (151 MHz, DMSO) (δ/ppm): 158.52, 155.92, 153.61, 150.52, 145.30, 141.50, 136.71, 132.27, 126.81, 125.67, 120.69, 120.66, 118.99, 116.94, 115.88, 111.51; Elemental analysis: Found: C, 56.8; H, 2.6; N, 8.3; O, 9.5%; molecular formula $C_{16}H_9BrN_2O_2$ requires: C, 56.5; H, 2.8; N, 8.0; O, 9.4%; MS (ESI): m/z = 342.01 ([M +1]$^+$, 344.02 ([M + 3]$^+$).

2.2. Spectroscopic Characterization

UV–Vis absorption spectra were recorded at room temperature on a Varian Cary 50 double-beam spectrophotometer in the 250–600 nm range. Measurements were performed in reagent-grade organic solvents using 1 cm quartz cuvettes at 0.1 nm intervals, with all samples at 2×10^{-5} M.

2.3. pH Titrations

The pH-dependent spectroscopic behavior of iminocoumarins was studied in universal buffers covering pH 1–13 at room temperature. For titrations, 0.1 M HCl and 0.1 M NaOH were used to provide extremely acidic and basic conditions. Compounds **11–13** were prepared at 2×10^{-5} M, and pK_a values were determined from absorption titrations by analyzing the wavelength of maximum absorbance under acidic conditions using the Boltzmann equation.

2.4. NMR Spectroscopy Analysis Under Varying pH Conditions

For measurements under slightly basic conditions, 2700 μL of DMSO-d$_6$ was combined with 300 μL of D_2O, yielding a pD of 8.3. After applying a 0.4-unit correction to account for the glass electrode response in D_2O, the effective pH was estimated at 8.7. Aliquots of

700 μL from this solution were used to dissolve 8.2 mg (**11**), 5.2 mg (**12**), and 6.7 mg (**13**), resulting in corrected pH values of 6.8 (**11**), 7.9 (**12**), and 6.2 (**13**).

For acidic conditions, 2700 μL of DMSO-d_6 was mixed with 300 μL of 1 M DCl in D_2O, giving a pD of 1.7. After correcting for the glass electrode response, the actual pH was estimated at 2.1. Compounds **11–13** were added to 700 μL aliquots of this solution in the following amounts: 7.6 mg (**11**), 5.1 mg (**12**), and 6.1 mg (**13**), resulting in corrected pH values of 2.2 for all three compounds.

Full ^{1}H and ^{13}C NMR assignments were obtained using one- and two-dimensional experiments (^{1}H, ^{13}C, COSY, HSQC, and HMBC). Spectra were recorded on a Bruker Avance AV300 spectrometer equipped with a 5 mm BBO probe and z-gradient accessory, employing standard Bruker pulse sequences (Bruker, Billerica, USA). Additional experimental details are provided in the Supplementary Information. All pH measurements were performed using a Metrohm 949 pH meter with a 6.0234.100 electrode (Metrohm, Herisau, Switzerland), and all deuterated solvents were obtained from EurIsotop (Saint-Aubin, France).

2.5. Computational Details

All molecular geometries were optimized at the B3LYP/6–311+G(d,p) level, which offers a suitable compromise between computational accuracy and efficiency. Thermal corrections to Gibbs free energies were obtained from unscaled harmonic vibrational frequencies, as is common in high-accuracy DFT thermochemistry and pK_a calculations with B3LYP to account for partial cancelation between harmonic overestimation and anharmonic effects. This approach contributes to the good agreement observed between computed and experimental pK_a values. Gas-phase energies were further refined via single-point calculations employing the larger 6–311++G(2df,2pd) basis set. Solvent effects were modeled using the SMD continuum approach for water, resulting in the B3LYP/6–311++G(2df,2pd)//(SMD)/B3LYP/6–311+G(d,p) protocol used in this study. This computational scheme has been previously validated for reproducing kinetic and thermodynamic parameters in organic [33] and biochemical [34] systems, as well as pK_a values of related organic derivatives [17,28]. The pK_a values were determined using an absolute approach, incorporating both the gas-phase free energy of the proton, $G(H^+) = 6.28$ kcal mol^{-1}, and its experimental solvation free energy in water, $\Delta G_{SOLV}(H^+) = -265.9$ kcal mol^{-1} [35], consistent with the SMD parameterization by Truhlar and co-workers [36]. A free energy correction of -1.89 kcal mol^{-1} was included to account for the conversion from a gas-phase pressure of 1 atm to a 1 M solution concentration. UV-Vis electronic transitions were computed using single-point (SMD)/CAM-B3LYP/6–311+G(d,p) calculations within the TD-DFT framework, considering the 64 lowest-energy singlet excitations. All computations were carried out using the Gaussian 16 software package [37].

2.6. Biological Activity

All biological assays were performed under standard conditions. The samples were not exposed to direct light during incubation, and microplates were kept in the dark inside the CO_2 incubator to exclude potential phototoxic effects.

2.6.1. Antiproliferative Activity In Vitro

Human cancer cell lines Capan-1, HCT-116, NCI-H460, LN-229, HL-60, K-562, and Z-138 were obtained from the American Type Culture Collection (ATCC), whereas the DND-41 cell line was sourced from the Deutsche Sammlung von Mikroorganismen und Zellkulturen (DSMZ). Cells were cultured in Gibco media with 10% fetal bovine serum. Adherent Capan-1 cells were seeded at 500 cells per well, and HCT-116, NCI-H460, and LN-229 cells at 1500 cells per well in 384-well plates. After overnight incubation, cells were treated with seven concentrations of the test compounds (0.006–100 µM). Suspension cell lines HL-60, K-562, and Z-138 were seeded at 2500 cells per well, while DND-41 cells were plated at 5500 cells per well in 384-well plates, using the same concentration series of test compounds. After 72 h, cell viability was measured using the CellTiter 96® AQueous One Solution (MTS) assay with final concentrations of 333 µg/mL MTS and 25 µM PMS, following the manufacturer's instructions.

2.6.2. Antiviral Activity In Vitro

Antiviral assays towards herpes simplex virus-1 (HSV-1 KOS, ATCC VR-1493), human coronavirus HCoV-229E (ATCC VR-740), and OC43 (ATCC VR-1558) in HEL 299 cells, respiratory syncytial virus A (ATCC VR-26) in Hep2 cell cultures, Sindbis virus (ATCC VR-1585), Yellow fever virus (17D-204, Stamaril), Zika virus (ATCC VR-1838), Semliki Forest virus (ATCC VR-67) in VeroE6 cells, human coronavirus (HCoV-NL63, obtained through the NIH Biodefense and Emerging Infections Research Resources Repository, NIAID (NR-470*)) in Hep3B cell cultures and influenza A/H1N1 (A/Ned/378/05, kindly provided by R. Fouchier), influenza A/H3N2 (A/HK/7/87, obtained from J. Neyts), influenza B (B/Ned/537/05, kindly provided by R. Fouchier) in MDCK cell cultures were performed. On the day of the infection, the growth medium was aspirated and replaced with serial dilutions of the tested compounds. The virus was then added to each well, diluted to a viral input of 100 $CCID_{50}$ ($CCID_{50}$ being the virus dose that infects 50% of the cell cultures). Mock-treated cultures receiving solely the test compounds were included to determine the cytotoxicity. After 3–7 days, depending on the virus, virus-induced cytopathogenic effects were quantified using the MTS assay (CellTiter 96® AQueous One Solution), with absorbance measured at 490 nm using a SpectraMax Plus 384 plate reader, and the optical density values were utilized to determine EC_{50} values. In parallel, the 50% cytotoxic concentration (CC_{50}) was derived from the mock-infected cells. The activities were compared with the activities of several reference antiviral drugs: remdesivir, chloroquine, ribavirin, zanamivir, rimantadine, dextran sulfate, Pro2000 and brivudine (BVDU).

2.6.3. Antifungal Activity In Vitro

An in vitro antifungal assay was evaluated following a modified literature procedure [38]. The analysis was performed on four phytopathogenic fungi (*Sclerotinia sclerotiorum*, *Macrophomina phaseolina*, *Botrytis cinerea*, and *Fusarium culmorum*), all from the collection of the Department of Phytopathology, Faculty of Agrobiotechnical Sciences Osijek. A volume of 1 mL of the compound stock solution (prepared by dissolving the appropriate mass of each compound in DMSO–water 30:70 *v/v* mixture) was added to 29 mL of potato dextrose agar (PDA), giving the final compound concentration of 0.08 µmol mL^{-1}, with the maintained DMSO volume fraction of 1%. Commercial fungicides were used as positive controls: strobilurin for *S. sclerotiorum* and *F. culmorum*, mancozeb for *M. phaseolina*, and fenhexamid for *B. cinerea*, and PDA with 1% DMSO as a negative control. Experiments were performed in quadruplicate. The Petri dishes were placed in a growth chamber set at 22 ± 1 °C under a 12 h light/12 h dark cycle, and radial mycelial growth was measured after 48 h. The inhibition effect of the compounds was expressed as the antifungal index (% mycelial growth inhibition).

3. Results and Discussion

3.1. Chemistry

Inspected benzoxazole iminocoumarins **11–16** were prepared according to Scheme 1.

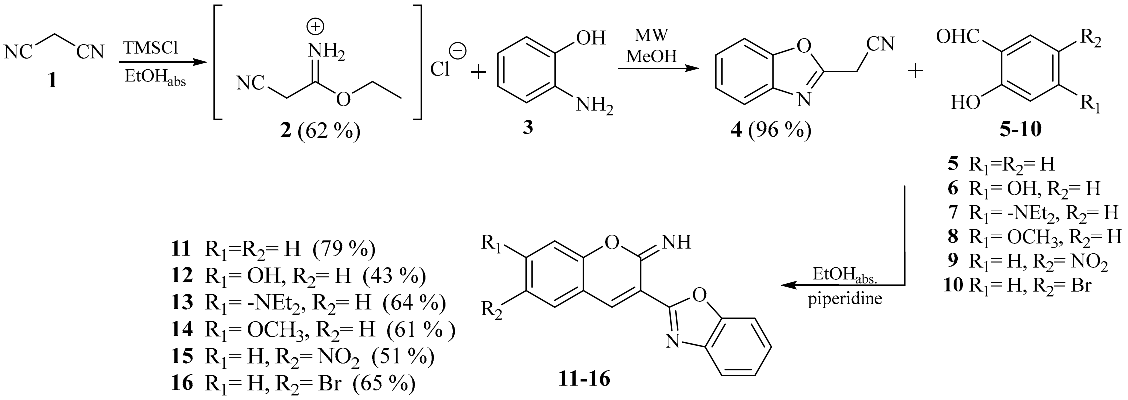

Scheme 1. Synthesis of benzoxazole-derived iminocoumarins **11**–**16**.

The main precursor, 2-cyanomethylbenzoxazole **4**, was synthesized in excellent yield (96%) via a microwave-assisted cyclocondensation (120 °C, 500 W) between commercially available *ortho*-aminophenol **3** and freshly prepared 2-cyanoacetimidic acid ethyl ester hydrochloride **2**. Microwave irradiation was employed for this cyclization step due to its well-documented advantages over conventional heating in similar heterocyclic syntheses, including dramatically shorter reaction times (often reduced from hours to minutes), higher energy efficiency, uniform volumetric heating, and frequently improved yields with fewer side products.

Precursor **2** was obtained through a facile Pinner-type condensation of malononitrile (**1**), chlorotrimethylsilane (TMSCl), and ethanol at 0 °C for 17 h [34,39–41]. There, HCl forms in situ from one equivalent of ethanol and TMSCl, followed by nucleophilic attack of the second ethanol equivalent to yield the white crystalline salt (**2**) [42]. Iminocoumarins **11**–**16** were synthesized using a previously optimized Knoevenagel condensation method developed in our group [17,28]. It begins with base-mediated methylene deprotonation in 2-cyanomethylbenzoxazole (**4**), generating a stabilized carbanion. The latter undergoes nucleophilic addition to salicylaldehyde, forming an oxyanion intermediate that cyclizes intermolecularly to close the iminocoumarin core. Subsequent dehydration and proton transfer yield a conjugated system stabilized by extended π-delocalization [43]. Equimolar amounts of **4** and the respective aromatic aldehydes were refluxed in absolute ethanol with a few drops of piperidine. Reactions were monitored by TLC and purified via column or flash chromatography using DCM/MeOH as eluent, affording moderate to good yields (38–79%). The unsubstituted analog **11** provided the highest yield, benefiting from the lack of electronic perturbations, while compound **15** (bearing a strongly electron-withdrawing NO_2 at C-6) gave the lowest, owing to intermediate destabilization and potential side reactions. At C-7, electron-donating substituents like methoxy or *N*,*N*-diethylamino slightly diminished carbonyl electrophilicity but supported intermediate stabilization, yielding good results overall. In contrast, a hydroxy group at C-7 led to a sharper yield drop, likely from hydrogen-bonding disruptions to the reaction pathway.

All products were characterized by ^{1}H and ^{13}C NMR, with assignments based on chemical shifts and vicinal coupling constants. Some signals were obscured by hydrogen bonding or deuterium exchange from the solvent. Precursor formation was evidenced by a CH_2 singlet at δ 4.70 ppm, while successful cyclization to **11**–**16** was indicated by its disappearance.

3.2. Spectroscopic Characterization

To investigate the spectroscopic properties of the prepared compounds **11**–**13**, UV-Vis absorption spectra were recorded in several organic solvents with different polarities. The

https://doi.org/10.3390/chemosensors14010015

main focus was to investigate the effect of the substituent placed on the coumarin nuclei as well as the effect of the solvent on spectroscopic features (Table S1).

UV-Vis spectra were recorded at room temperature in the range of 250–600 nm using high-purity solvents with varying polarity parameters: Milli-Q water, methanol, ethanol, ethyl acetate, acetonitrile, and toluene [44]. The absorption spectra are presented in Figure 2a,c, with a comparison of UV-Vis spectra in one polar protic solvent (methanol) and one nonpolar solvent (toluene) shown in Figure 2d, with dominant absorption bands attributed to π–π* electronic transitions, as confirmed by computational natural transition orbital analysis (Figures S13–S15).

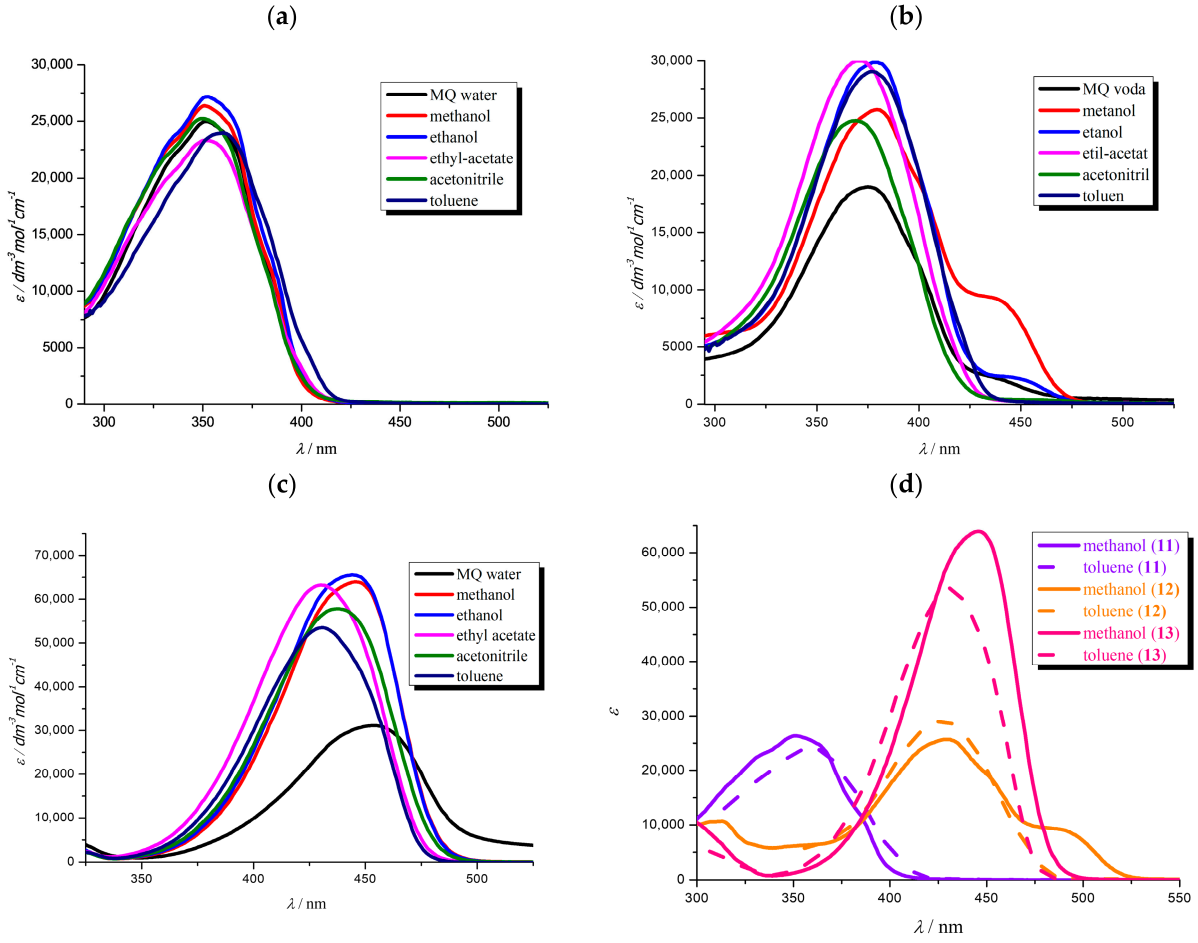

Figure 2. UV-Vis spectra of **11** (**a**), **12** (**b**) and **13** (**c**) at $c = 2 \times 10^{-5}$ mol dm^{-3} in several solvents with different polarity; compared spectra of **11**–**13** in toluene and methanol (**d**).

Compound **11** exhibited a single main absorption band in all tested solvents. A slight increase in absorption intensity was observed in ethanol compared to the other solvents, indicating a minor hyperchromic shift, whereas the absorbance was lowest in ethyl acetate. In toluene, **11** displayed a slight bathochromic shift in the absorption maximum relative to the other solvents.

Molecule **12** showed a single main absorption band in the range of 325–425 nm in all solvents except ethanol and methanol, where an additional maximum appeared at approximately 450 nm. The highest absorbance intensity was observed in ethyl acetate, accompanied by a slight hypsochromic shift in the absorption maximum relative to the other solvents. The most pronounced hypsochromic shift for **12** was observed in acetonitrile, accompanied by a hypochromic shift compared to ethyl acetate. UV-Vis spectra of **11**–**13** in methanol and ethanol were compared. Methanol and ethanol were selected

https://doi.org/10.3390/chemosensors14010015

as closely related polar protic solvents to evaluate the influence of subtle differences in solvent polarity and hydrogen-bonding ability. The observed minor spectral shifts indicate that the absorption behavior of these systems is sensitive to specific solute–solvent interactions in addition to the electronic nature of the substituents. At 378 nm, **12** exhibited a significant hyperchromic shift in ethanol relative to methanol, while at approximately 440 nm, it showed a more pronounced hypochromic shift with a slight bathochromic shift in ethanol compared to methanol. The somewhat lower molar absorption coefficients observed in methanol can be attributed to the coexistence of neutral and partially deprotonated species in equilibrium, resulting in reduced overall absorbance. This explanation is consistent with the protonation–deprotonation behavior evidenced by our pH-dependent spectroscopic and computational analyses, and it is expected that the addition of a small amount of acid would shift the equilibrium toward the neutral form, yielding absorption coefficients similar to those measured in toluene. In water, **12** and **13** displayed the lowest absorption intensities.

Compound **13** exhibited the most significant hypochromic shift in water, accompanied by the most pronounced bathochromic shift. The highest increase in absorption intensity for **13** was observed in ethanol, whereas a hypsochromic shift was observed in ethyl acetate. Figure 2d compares absorption spectra of **11**–**13** in toluene and methanol. Based on these spectra, the type of substituent on the coumarin nucleus significantly influences the spectroscopic properties. The unsubstituted **11** showed a significant hypsochromic shift in its absorption maximum in both polar (methanol) and nonpolar (toluene) solvents relative to **12** and **13**. In methanol, **11** exhibited a slight hypsochromic shift and a hyperchromic shift compared to toluene. The substituted **12** and **13** displayed significant bathochromic shifts in their absorption maxima. Compound **13**, substituted with the strong electron-donating *N*,*N*-diethylamino group, exhibited bathochromic shifts in both solvents, with the most significant bathochromic shift and hyperchromic shift observed in methanol. This behavior can be attributed to the strong electron-donating character of the *N*,*N*-diethylamino group, which enhances intramolecular charge transfer in polar solvents, resulting in increased absorption intensity (hyperchromic effect). In contrast, the hydroxy-substituted **12** exhibited stronger absorption intensity in toluene compared to methanol, which can be attributed to reduced solvation and hydrogen-bonding interactions in nonpolar media. This environment enhances the resonance contribution of the phenolic –OH group and facilitates intramolecular charge transfer, resulting in increased absorption intensity [45,46].

Compounds **14**–**16**, bearing methoxy, nitro, and bromo substituents on the coumarin nucleus, were synthesized analogously to **11**–**13**. Although detailed spectroscopic measurements were not performed, their optical properties are expected to follow the same structure–property relationships observed for **11**–**13**. In particular, substitution with an electron-donating methoxy group (**14**) would be anticipated to induce a slight bathochromic shift, whereas electron-withdrawing substituents (NO_2, Br) in **15** and **16** are expected to cause modest hypsochromic shifts relative to the parent compound **11**.

Although no pronounced color change was observed within the studied pH range, the recorded and computationally supported pH-dependent spectral shifts (see latter) clearly demonstrate the optical responsiveness of the investigated systems, supporting their potential as pH-sensitive materials. Preliminary fluorescence screening revealed only weak emission for all compounds, consistent with dominant nonradiative deactivation pathways arising from intramolecular charge transfer within the extended π-conjugated system; therefore, detailed fluorescence studies were not pursued further.

3.3. Effects of pH on Spectral Properties

The acid–base properties of compounds **11–13**, which govern their potential as optical pH probes, arise from distinct protonation/deprotonation sites within the benzoxazole-iminocoumarin scaffold. These sites were identified computationally (Section 3.4) and drive reversible spectral responses via altered π-conjugation and charge transfer.

The potential of compounds **11–13** to function as optical pH probes was evaluated by monitoring changes in their spectroscopic properties under varying pH conditions through spectroscopic pH titrations. To assess the acid-base properties, aqueous pK_a values were determined from the recorded spectroscopic data, based on the optical quantification of the acidic (HA) and basic (A^-) species using the Henderson–Hasselbalch equation [47,48]:

$$pH = pK_a + \log\frac{[\mathrm{A}^-]}{[\mathrm{HA}]}$$

The variation in pH conditions enabled the protonation and deprotonation of the investigated systems, accompanied by a reorganization of electron density within their structures. As a result, pronounced changes were observed in the absorption spectra, supporting their potential application as optical pH probes (Figure 3). The spectroscopic properties during pH titrations for compounds 11–13 are presented in Table 1. The pK_a values were determined as the inflection point of a sigmoid Boltzmann curve fitted to the experimental pH titration data (Figure S17).

Table 1. pH dependence of absorption features of **11–13** in buffered aqueous solutions.

	λ_a (nm)			$\varepsilon \times 10^3$ (dm^3 mol^{-1} cm^{-1})				
	Acidic [a]	Neutral [b]	Basic [c]	Acidic	Neutral	Basic	p$K_{a(exp)}$	p$K_{a(calc)}$
11	351	351	311 396	24.90	34.90	19.10 19.20	11.0	12.8
12	259 380	276 427	276 427	7.90 20.55	13.05 36.45	8.65 42.75	4.8	4.7
13	317 349 496	287 453	285 443	12.20 10.30 60.85	11.05 36.45	11.95 44.05	13.0	13.5

[a] 0.1 M HCl; [b] MQ water; [c] Buffer at pH = 13.

In acidic and neutral media, compound **11** showed a single absorption maximum at approximately 350 nm. However, upon increasing the pH, significant spectral changes were observed. Specifically, at pH 11.03, a decrease in absorption maximum was observed, resulting in a significant hypochromic shift. At pH 12.02 and 13.06 two new absorption maximum appeared at approximately 310 and 395 nm, with hyperchromic shifts at pH 13.06. These changes suggest that at higher pH values (pH $\geq$ 12), complete deprotonation induces the formation of anionic species with modified π-conjugation, leading to new chromophore systems and distinct absorption bands. The reduced absorption intensity at pH 11.03 likely reflects the dynamic equilibrium between the neutral and monoanionic forms, resulting in spectral broadening. New absorption maximum at pH 12.02 and 13.06 indicate the presence of spectroscopically different, fully deprotonated species.

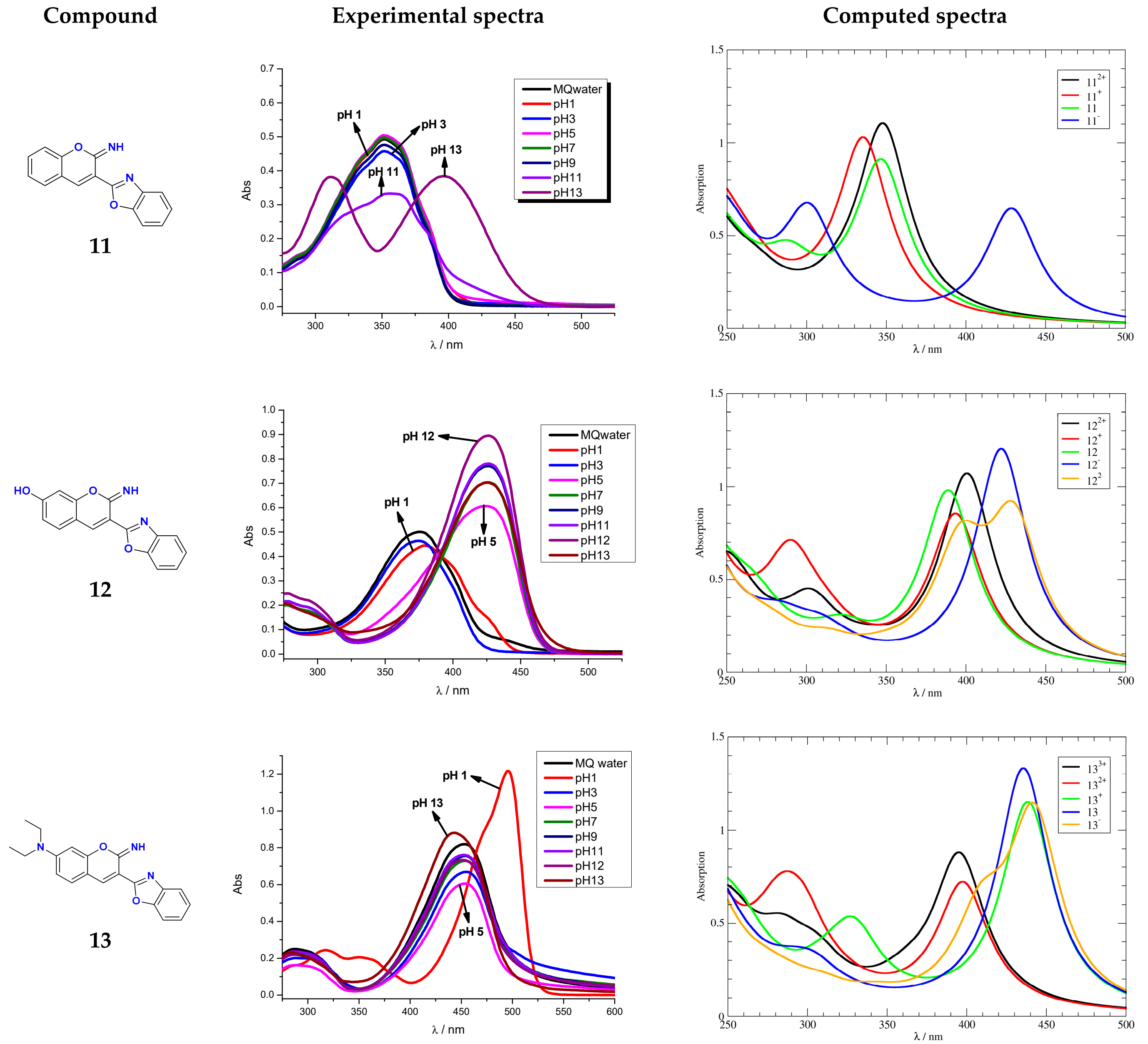

Figure 3. Absorption spectra of **11**–**13** at different pH values in buffer together with spectra computed with the (SMD)/CAM-B3LYP/6–311+G(d,p) model in water. Related displays illustrating the dependencies of absorption on pH are presented as Figure S16.

Compound **12**, with a hydroxy substituent on the iminocoumarin core, showed two absorptions maxima in acidic medium: one in the region of 250–300 nm and a more intense one between 350 and 450 nm. At pH 6.08, a bathochromic shift in both absorption maxima was observed, accompanied by a slight hyperchromic effect, especially pronounced at 400 nm, where peak broadening was also visible. Further increase in pH value led to a continuous increase in absorption intensity, resulting in substantial hyperchromic shifts with notable bathochromic shifts in both absorption maxima. These spectral changes can be attributed to the deprotonation of the OH group, which resulted in enhanced π-conjugation and increased intramolecular charge transfer. The most pronounced hyperchromic shift was detected at pH 10.95. The system showed a gradual hyperchromic shift in the pH range 6–11, after which a decrease in absorption intensity was observed.

Compound **13**, substituted with a strong electron-donating *N,N*-diethylamino group, showed two absorption maximum, one around 300 nm and a more intense one around 450 nm. Under strongly acidic conditions (pH 1.05), a pronounced bathochromic shift in both absorption maxima was observed, accompanied with a strong hyperchromic shift at 500 nm. This behavior can be attributed to structural degradation or protonation-induced perturbations of the chromophore in highly acidic media. At other pH values, the compound did not reveal any major spectral shifts. The most significant hypochromic effect was seen at pH 5.00, while at pH 13.06, a noticeable hyperchromic shift was recorded, accompanied by a slight hypsochromic shift in the absorption maximum. The described changes can be primarily ascribed to the acid/base equilibria of the *N,N*-diethylamino group—protonation in acidic media suppresses its electron-donor ability, while unionized forms at intermediate pH support enhanced conjugation and stronger absorption. Acid-base properties of **11–13** are characterized by an "apparent" pK_a value, and our method allowed us to identify a single value for all compounds (Table 1).

3.4. Computational Analysis

We employed computational DFT analysis to determine the dominant protonation forms of each system that influence alterations in photophysical properties under different pH conditions. The B3LYP/6–311++G(2df,2pd)//(SMD)/B3LYP/6–311+G(d,p) model was used to calculate pK_a values in the aqueous phase (Table 2), while the TD-DFT approach at the (SMD)/CAM-B3LYP/6–311+G(d,p) level predicted UV-Vis spectra for each protonation state (Figure 3).

Table 2. Computed pK_a values by the B3LYP/6–311++G(2df,2pd)//(SMD)/B3LYP/6–311+G(d,p) model in water and their comparison with experiments reported in this work.

Compound	Protonation Forms	Process	p$K_{a,CALC}$	p$K_{a,EXP}$
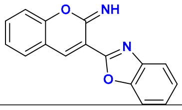	$\mathbf{11^{+}} \longrightarrow \mathbf{11^{2+}}$	benzoxazole N protonation	−1.4	
	$\mathbf{11} \longrightarrow \mathbf{11^{+}}$	iminocoumarin N protonation	4.1	
	$\mathbf{11} \longrightarrow \mathbf{11^{-}}$	iminocoumarin N deprotonation	12.8	11.0
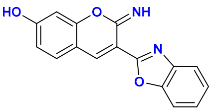	$\mathbf{12^{+}} \longrightarrow \mathbf{12^{2+}}$	benzoxazole N protonation	−1.3	
	$\mathbf{12} \longrightarrow \mathbf{12^{+}}$	iminocoumarin N protonation	4.7	4.8
	$\mathbf{12} \longrightarrow \mathbf{12^{-}}$	–OH deprotonation	10.4	
	$\mathbf{12^{-}} \longrightarrow \mathbf{12^{2-}}$	iminocoumarin N deprotonation	13.2	
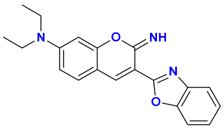	$\mathbf{13^{2+}} \longrightarrow \mathbf{13^{3+}}$	benzoxazole N protonation	0.6	
	$\mathbf{13^{+}} \longrightarrow \mathbf{13^{2+}}$	aniline N protonation	2.7	
	$\mathbf{13} \longrightarrow \mathbf{13^{+}}$	iminocoumarin N protonation	7.6	
	$\mathbf{13} \longrightarrow \mathbf{13^{-}}$	iminocoumarin N deprotonation	13.5	13.0

The molecules under investigation consist of a benzoxazole unit linked to an iminocoumarin fragment. In this context, it is relevant to highlight the experimental pK_a values for model systems pertinent to this study (Figure 4). Unsubstituted benzoxazole is a very weak base, requiring highly acidic conditions for protonation. Notably, protonation occurs on the nitrogen atom, consistent with our results, which predict that protonation on nitrogen is 38.6 kcal mol^{-1} more favorable than on the oxygen atom. The basicity of benzoxazole can be enhanced by 2-alkylation, as seen in our investigated systems, with 2-methylbenzoxazole exhibiting a pK_a of approximately 1. This value suggests protonation is potentially achievable under our experimental conditions. In contrast, aromatic amines are weaker bases than their aliphatic counterparts, yet the basicity of *N,N*-diethylaniline, with a pK_a of 6.9, indicates that protonation is likely under our measurement conditions.

Furthermore, phenol deprotonation typically occurs at a pH of approximately 10 and is expected in our experiments. Although precise literature data on the acid/base properties of the iminocoumarin moiety are unavailable, the pK_a of 2-oxazoline (5.5) suggests that iminocoumarin is significantly more basic than benzoxazole and comparable in basicity to dialkylanilines. In summary, under our experimental conditions, we anticipate protonation of aniline and iminocoumarin, deprotonation of phenol, and potential acid/base exchange involving benzoxazole.

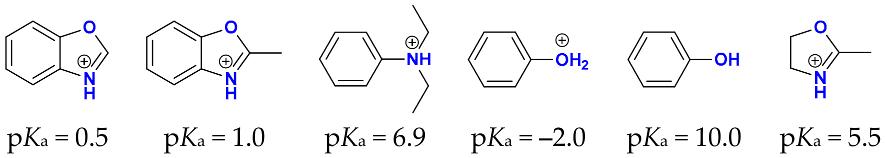

Figure 4. Experimental pK_a values for the relevant model compounds [49,50].

Molecule **11** represents the simplest system, with unsubstituted benzoxazole and iminocoumarin directly linked. The iminocoumarin nitrogen is the most basic site, computed as pK_a = 4.1. Protonation at this site is favored over the benzoxazole nitrogen by 10.0 kcal mol^{-1}, rendering the latter negligible for the first protonation. Thus, under neutral conditions, **11** remains unionized in aqueous solution. Interestingly, the first protonation significantly reduces the benzoxazole basicity, resulting in a pK_a of –1.4, which is unlikely to be fully achieved under our experimental conditions (pH 1–13). However, at the lowest pH values, particularly around pH $\approx$ 2 used in NMR measurements (see later), a small percentage of the diprotonated species (**11**$^{2+}$) exists, with the additional proton residing on the benzoxazole nitrogen. This observation is relevant for interpreting NMR data in the following paragraph. In contrast, iminocoumarin deprotonation is calculated to have a pK_a of 12.8, aligning with the experimental value of 11.0. We observed that this process triggers a spontaneous C–O bond cleavage, decomposing the system into an acrylonitrile derivative (Scheme 2) during geometry optimization. This behavior is analogous across all systems **11–13**.

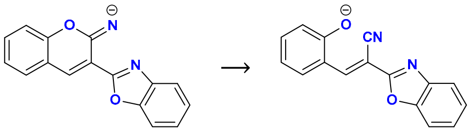

Scheme 2. Spontaneous degradation of **11** following iminocoumarin deprotonation at pK_a = 11, analogously observed in **12** and **13**.

UV-Vis spectra of **11** corroborate its protonation behavior. The computed absorption maximum for neutral **11** at 347 nm closely matches the experimental value of 350 nm at pH 7, confirming its predominance under normal conditions. Notably, the absorption maxima for the cationic **11**$^{+}$ (monoprotonated at iminocoumarin) and **11**$^{2+}$ (diprotonated at benzoxazole), exhibit significant overlap, with maxima at 335 and 348 nm. This explains why both protonation equilibria are indistinguishable in the UV-Vis spectra and justifies the inability to experimentally determine these pK_a values with this technique. In contrast, the transition from **11** to **11**$^{-}$ (deprotonated at iminocoumarin) is clearly observed in the UV-Vis spectra at high pH values. The computed absorptions at 300 nm and 428 nm for **11**$^{-}$ align with experimental 310 and 395 nm, thus confirming the ring-opening (Scheme 2). Thus, our experiments capture the neutral-to-monodeprotonated transition at pK_a 11.0, while iminocoumarin and potential benzoxazole protonations remain undetectable.

The introduction of an –OH group on iminocoumarin in **12** modifies its acid-base features, though not significantly for the protonation processes analogous to those in

11. The computed pK_a values for iminocoumarin and benzoxazole protonation remain largely unchanged at 4.7 and -1.3, the former in excellent agreement with measured 4.8. Absorption maxima of 394 nm for $\mathbf{12^{+}}$ confirms its presence under acidic conditions (380 nm experimentally), while 401 nm for $\mathbf{12^{2+}}$, even if achieved in our experiments, suggests a high overlap with $\mathbf{12^{+}}$. In contrast, the phenolic –OH group is considerably more acidic than the iminocoumarin N–H, with a computed pK_a of 10.4 making it the most acidic site in **12**, while the iminocoumarin deprotonation shifts to pK_a = 13.2. The computed absorption maxima for monodeprotonated $\mathbf{12^{-}}$ (422 nm) and dideprotonated $\mathbf{12^{2-}}$ (430 nm) also overlap, rendering their interconversion undetectable by UV-Vis spectroscopy. Nevertheless, their positions closely match a series of experimental spectral lines observed around 420 nm. Yet, the existence of a line at 396 nm for $\mathbf{12^{2-}}$, absent in the experimental spectra, likely suggests this form is beyond the employed conditions.

Compound **13** is the most intriguing, as its experimental UV-Vis spectra show significant overlap of absorption maxima centered around 450 nm across pH 2–13, with a pronounced shift to approximately 500 nm under highly acidic conditions (pH 1). Our DFT analysis indicates that iminocoumarin deprotonation occurs at a pK_a of 13.5, in good agreement with the experimental value of 13.0. However, although the iminocoumarin moiety is intrinsically less basic than the diethylaniline group, the iminocoumarin nitrogen remains the most basic site in **13**, with its basicity surpassing that of diethylaniline by 14.8 kcal mol^{-1}. The computed pK_a of 7.6 for the iminocoumarin protonation reflects the strong electron-donating effect of the diethylamino group, which stabilizes iminocoumarin protonation through resonance rather than accommodating the proton itself. In addition, such a basicity enhancement makes monoprotonated $\mathbf{13^{+}}$ a predominant form at neutral pH, offering a significant difference over **11** and **12**. This feature reduces the aniline basicity to pK_a = 2.7, though it remains the preferred site for the second proton after iminocoumarin. Notably, in $\mathbf{13^{+}}$, the basicity of aniline exceeds that of the benzoxazole nitrogen by only 0.1 kcal mol^{-1}, making both sites nearly equivalent for the second protonation. However, explicit calculation of the pK_a for the third protonation of $\mathbf{13^{2+}}$ predicts a value of 0.6 for benzoxazole protonation, which is readily achievable under the most acidic conditions considered (pH 1). Consequently, the 0.4-unit difference between the experimental pH and the computed pK_a suggests that approximately 40% of the triprotonated $\mathbf{13^{3+}}$ species is present in solution at pH 1, which is highly relevant for interpreting the photophysical properties under such acidic conditions.

These conclusions are supported by the agreement between computed UV-Vis absorption maxima at 438 nm for $\mathbf{13^{+}}$, 436 nm for neutral **13**, and 442 nm for $\mathbf{13^{-}}$ that are all found within a narrow 16 nm range, thus tying in with experiments across pH 2–13. However, the computed UV-Vis transitions for the subsequently protonated $\mathbf{13^{2+}}$ and $\mathbf{13^{3+}}$ predict absorptions at 398 and 395 nm that are both absent in the experimental spectra (Figure 3). This confirms that once the solution conditions become acidic enough, the protonation at both diethyamine and benzoxazole occurs simultaneously or very closely apart. On the other hand, when the benzoxazole nitrogen is protonated, it can undergo a hydrolytic ring-opening reaction via C–O or C–N bond fission [51,52]. This process explains the absence of the expected absorptions for $\mathbf{13^{2+}}$ and $\mathbf{13^{3+}}$, and confirms the degradation of the later. Our results (Table 3) indicate that the C–O fission pathway is thermodynamically much favored in all derivatives **11**–**13**, suggesting the predominance of the amide (rather than ester) derivative in solution under highly acidic conditions. This finding is consistent with literature reports demonstrating the prevalence of the amide-containing derivatives in various benzoxazoles under highly acidic conditions [53,54].

Table 3. Reaction Gibbs free energies for the hydrolytic degradation of **11**–**13** by C–N and C–O fission pathways, obtained by the (SMD)/B3LYP/6–311+G(d,p) model in water.

Reactant	Product	Reaction Gibbs Free Energy (ΔG_R)
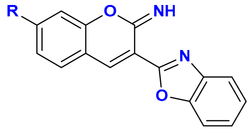	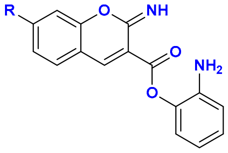 C–N Fission Product	11.6 kcal mol^{-1} (**11**, R = –H) 12.0 kcal mol^{-1} (**12**, R = –OH) 10.2 kcal mol^{-1} (**13**, R = –NEt$_2$)
	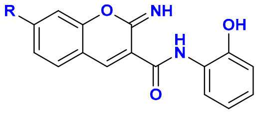 C–O Fission Product	1.3 kcal mol^{-1} (**11**, R = –H) 1.7 kcal mol^{-1} (**12**, R = –OH) 0.4 kcal mol^{-1} (**13**, R = –NEt$_2$)

Comparison of the computed UV-Vis spectra for **13^{3+}** and its C–N and C–O fission degradation products (Table 3) reveals that the benzoxazole ring opening offers products with notably blue-shifted maxima (Figure 5), 333 nm for the favored C–O fission product, and 306 nm for the less favorable C–N fission alternative. This trend is consistent with the reduced π-electron conjugation in both products, which decreases delocalization and increases the energy gap between the ground and excited states, requiring shorter wavelengths to achieve the electronic transition. Yet, their absence in the measured spectra confirm long time scales required for their formation, exceeding those employed for the immediate UV-Vis measurements. In addition, neither degradation product accounts for the experimental absorptions at arround 500 nm at pH 1, the precise origin of which presently remains unclear. We tentatively attribute this transition to aggregation effects, charge-transfer complexes, or the formation of further degradation products with extended conjugated π-systems, though their precise identification is beyond the scope of this study.

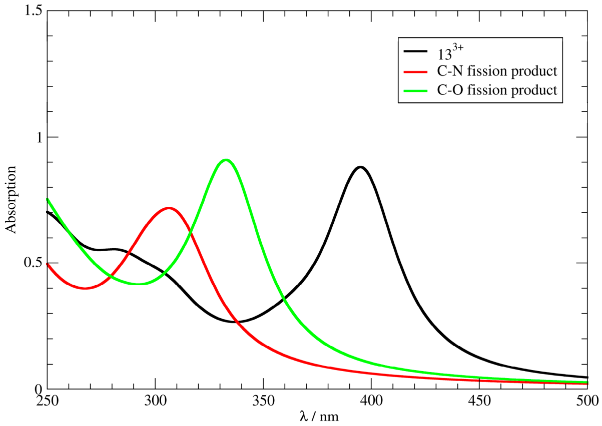

Figure 5. Computed UV-Vis spectra for diprotonated **13^{2+}** and its hydrolitic degradation products obtained by the (SMD)/CAM-B3LYP/6–311+G(d,p) model in water.

3.5. Probing the Protonation Equilibria with NMR Spectroscopy

Compounds **11**–**13** were subjected to NMR analysis to confirm the protonation sites under strongly acidic conditions. For each system, two sets of samples were prepared: one under neutral/basic conditions (pH = 6–8) and the other under highly acidic conditions (pH = 2.2). The obtained NMR spectra under both conditions are summarized in Table S2.

The NMR spectra of samples under acidic conditions at 25 °C showed no direct evidence of protonation. Instead, all three compounds underwent a slow chemical transformation, which was not fully completed even after one month. The latter aligns with the presented thermodynamic consideration of the hydrolytic degradation route (Table 3), which highlighted the endergonic character of all transformations, suggesting only moderate product yields. The NMR spectra of those reaction mixtures were recorded and used to determine the structures of the newly formed products named **11H–13H** (Figure 6), confirming the feasibility of the C–O fission pathway. Since the prerequisite for cleavage of the benzoxazole ring is activation of the benzoxazole nitrogen through protonation, the generation of identified hydrolytic products provides direct evidence that such highly acidic conditions involve protonation at this position.

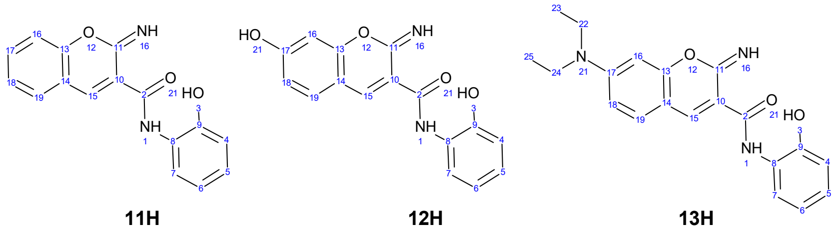

11H **12H** **13H**

Figure 6. The structures of C-O (amide) fission products of hydrolysed benzoxazoles.

3.6. Multifunctional Potential: Preliminary Biological Evaluation

Building on the substituent-dependent photophysical tuning observed in previous sections, where electron-donating groups (e.g., in **13**) enhance intramolecular charge transfer and solubility, these hybrids were screened for antiproliferative, antiviral, and antifungal activities in vitro to assess their broader biomedical utility.

3.6.1. Antiproliferative Activity In Vitro

Antiproliferative assays against a panel of human cancer cell lines, LN-229 (glioblastoma), Capan-1 (pancreatic adenocarcinoma), HCT-116 (colorectal carcinoma), NCI-H460 (lung carcinoma), DND-41 (acute lymphoblastic leukemia), HL-60 (acute myeloid leukemia), K-562 (chronic myeloid leukemia), and Z-138 (non-Hodgkin lymphoma), and normal PBMCs revealed structure-activity trends aligned with spectroscopic substituent effects. Compound **13** exhibited potent, broad-spectrum cytotoxicity (IC_{50} = 0.02–0.075 μM), though non-selective (PBMC IC_{50} = 0.08 μM), limiting its therapeutic potential without further structural optimization or targeted delivery strategies. Such a potent cytotoxicity aligns with prior reports on this derivative, where it exhibited sub-micromolar activity against ovarian, lung, bladder, and cervical cancer lines [29], underscoring the role of the electron-donating *N*,*N*-diethylamino group in enhancing membrane interactions and apoptosis induction. In contrast, electron-withdrawing nitro (**15**) and bromo (**16**) derivatives showed moderate, selective inhibition of leukemia lines (DND-41/HL-60 IC_{50} = 42–73 μM), and potential for targeted DNA intercalation without off-target effects on normal cells, thereby suggesting opportunities for further tuning selectivity, as explored in related metal complexes [30]. Unsubstituted **11** and methoxy **14** were inactive (IC_{50} > 100 μM). Full IC_{50} values are in Tables 4 and S3.

Table 4. In vitro antiproliferative activity (IC_{50} values) of iminocoumarins **11**–**16** against selected human cancer cells and cytotoxicity towards normal peripheral blood mononuclear cells (PBMC).

Cpd	**IC$_{50}$ (µM)**								
	Cell Lines								
	Capan-1	**HCT-116**	**LN-229**	**NCI-H460**	**DND-41**	**HL-60**	**K-562**	**Z-138**	**PBMC**
11	>100	>100	>100	>100	>100	>100	>100	>100	>100
12	>100	>100	>100	>100	>100	87.3	>100	>100	>100
13	0.05	0.02	0.045	0.075	0.03	0.02	0.06	0.02	0.08
14	>100	>100	>100	>100	>100	>100	>100	>100	>100
15	>100	>100	>100	>100	42.2	45.6	>100	>100	>100
16	>100	>100	>100	>100	70.7	73.0	>100	>100	>100
ETO	0.3	1.3	5.8	1.2	0.04	0.46	5.22	0.57	>10
NOC	0.03	0.03	0.14	0.12	0.04	0.46	5.22	0.57	>1

3.6.2. Antiviral Activity In Vitro

Antiviral potential of derivatives **11**–**16** was screened against a panel of clinically relevant RNA/DNA viruses (Table S3). The results are expressed as CC_{50} (50% cytotoxic concentration) and EC_{50} (50% effective concentration) values. None of the tested compounds exhibited significant antiviral activity across the evaluated viruses. Moreover, several derivatives demonstrated cytotoxic effects in host cell lines, further limiting their therapeutic applicability in this context.

3.6.3. Antifungal Activity In Vitro

Antifungal assays against agricultural phytopathogens [55–57] (*Sclerotinia sclerotiorum*, *Macrophomina phaseolina*, *Botrytis cinerea*, and *Fusarium culmorum*) at 0.08 µmol mL^{-1} showed moderate inhibition (up to 49.8% for 16 vs. B. cinerea), with electron-withdrawing and methoxy groups (**14**–**16**) outperforming others, consistent with prior coumarin antifungals where such substituents disrupt fungal membranes. All tested compounds showed lower activities over commercial fungicides (strobilurin, mancozeb, and fenhexamid) that served as positive controls and achieved around 90% inhibition (Table 5). These results are consistent with previous findings, where iminocoumarin derivatives exhibited moderate to low or no activity against pathogenic fungi [58]. Among the tested compounds, **16** with electron-withdrawing substituent, showed the highest inhibition, in line with earlier reports on coumarin derivatives [59,60].

Table 5. Percentage of mycelial growth inhibition (%) of the phytopathogenic fungi 48 h after inoculation with iminocoumarins **11**–**16** at 0.08 µmol mL^{-1} concentration (results expressed as the mean of four replicates ± standard deviation).

Cpd	**% Growth Inhibition After 48 h**			
	S. sclerotiorum	***M. phaseolina***	***B. cinereal***	***F. culmorum***
11	21.35 ± 3.56	18.46 ± 0.00	9.23 ± 5.22	4.47 ± 2.23
12	/	8.12 ± 2.95	17.53 ± 7.60	12.30 ± 5.17
15	/	30.28 ± 2.41	23.99 ± 6.74	4.47 ± 2.23
16	/	34.71 ± 1.71	49.82 ± 4.26	3.36 ± 2.65
14	/	33.97 ± 2.83	37.82 ± 7.61	8.95 ± 2.24
13	/	19.20 ± 3.72	2.77 ± 1.85	5.59 ± 2.58
negative control	0.00 ± 0.00	0.00 ± 0.00	0.00 ± 0.00	0.00 ± 0.00
positive control	93.00 ± 0.00 strobilurin	88.00 ± 0.00 mancozeb	84.00 ± 0.00 fenhexamid	87.50 ± 0.00 strobilurin

Although the biological results were moderate, their inclusion provides preliminary insight into the biological potential of the synthesized benzoxazole-iminocoumarins. These data complement the spectroscopic findings by highlighting the multifunctional character of the scaffold and suggest that further structural optimization could enhance both optical and biological performance.

3.6.4. Comparison with Literature Systems

Benzoxazole-containing heterocycles have been widely explored in medicinal chemistry, and several related systems have been evaluated for antiproliferative and antimicrobial activities. For example, a series of 3-(benzoxazol-2-yl)-2*H*-chromen-2-imine derivatives exhibited potent cytotoxic activity against multiple human cancer cell lines, with the most active compound showing IC_{50} values as low as < 0.01–0.30 μM against A-427 (ovarian), LCLC-103H (lung), RT-4 (bladder), and SISO (cervical) cancer lines; this performance is at the high potency end reported for benzoxazole–coumarin hybrids [30].

In other benzoxazole series, several derivatives demonstrated promising antimicrobial and antiproliferative effects, with MIC values comparable to standard controls against bacterial and fungal species, and selective anticancer effects against HCT-116 colorectal carcinoma cells [61]. Additionally, substituted benzoxazole–coumarin hybrids designed as carbonic anhydrase inhibitors exhibited mid-nanomolar K_i values toward tumor-associated isoforms (IX and XII), indicating that tailored substituent effects can yield both strong target engagement and selectivity in vitro [62].

While the absolute potencies vary across structural classes and assay conditions, the present compounds share structural features associated with structure–activity trends seen in prior work (e.g., enhanced activity with electron-donating substituents or specific steric profiles). Importantly, the integration of optical pH-responsive behavior with biological evaluation in a single structural platform distinguishes the current series from many classical benzoxazole or coumarin derivatives, which have generally been studied for one property domain at a time. This multifunctional characteristic positions our system as a promising scaffold for future optimization toward both sensing and therapeutic applications.

4. Conclusions

Novel benzoxazole-iminocoumarin hybrids (**11**–**16**) were efficiently synthesized via Knoevenagel condensation, yielding multifunctional heterocycles with tunable photophysical and biological properties. UV-Vis analysis in solvents of varying polarity revealed dominant π–π^* transitions with pronounced solvatochromic effects, influenced by substituents: unsubstituted **11** showed a ~350 nm band with minor hyperchromic shifts in protic media; hydroxy-substituted **12** exhibited dual maxima (~350/450 nm) and hypsochromic shifts in aprotic solvents; and *N*,*N*-diethylamino derivative **13** displayed the strongest bathochromic/hyperchromic responses (up to 453 nm in methanol), driven by enhanced intramolecular charge transfer.

pH titrations confirmed reversible spectral shifts, establishing **11**–**13** as viable optical probes: deprotonation of **11** induced hypochromic shifts and new bands (310/395 nm) at pH > 11; phenolic deprotonation in **12** caused bathochromic/hyperchromic changes peaking at 427 nm; and amine modulation in **13** yielded protonation-induced red-shifts at low pH and hypsochromic effects at high pH. DFT calculations accurately reproduced these behaviors, pK_a values, and degradation pathways, including iminocoumarin ring-opening upon deprotonation and preferential C–O fission in benzoxazole under acidic conditions, corroborated by NMR.

Biologically, **13** exhibited potent, non-selective nanomolar cytotoxicity across cancer lines, while **15** and **16** showed moderate, selective activity against leukemias. Limited antifungal inhibition was noted for **14–16** against phytopathogens, with no antiviral efficacy.

These findings highlight benzoxazole-iminocoumarins as versatile scaffolds for pH chemosensing and bioactive agents. Future efforts will target substituent optimization to enhance selectivity and stability, enabling advanced optical probes and targeted therapeutics.

Supplementary Materials: The following supporting information can be downloaded at: https://www.mdpi.com/article/10.3390/chemosensors14010015/s1, Figures S1–S12: NMR spectra of prepared compounds, Figures S13–S15: Computed UV-Vis spectra for **11**–**13** at pH = 7 together with graphical representation of natural transition orbitals for the dominant excitation, Table S1: Spectroscopic data for **11**–**13**, Figures S16–S17: Dependencies of UV-Vis absorption intensity on pH conditions for **11**–**13** and Boltzmann fitting curves used for the calculations of the pK_a values, Table S2: Comparison of chemical shifts for **11**–**13** with their hydrolyzed products under acidic conditions, Figures S18–S47: NMR spectra of compounds **11**–**13** and their hydrolyzed products under acidic conditions, Table S3: Cytotoxicity and antiviral activity in vitro for **11**–**16**. Table S4: Mass spectra for **11**–**16**.

Author Contributions: Conceptualization, M.K., D.D., M.H. and R.V.; Formal Analysis, M.G., A.Č., L.P., K.V. and R.V.; Investigation, M.G., A.Č., L.P., K.V., M.K., M.H. and R.V.; Writing—Original Draft Preparation, A.Č., L.P., M.K., M.H. and R.V.; Supervision, D.D., M.K., M.H. and R.V.; Funding Acquisition, M.H. and R.V. All authors have read and agreed to the published version of the manuscript.

Funding: This work was supported by the Croatian Science Foundation under the projects IP-2024-05-7208 and IP-2020-02-8090.

Data Availability Statement: Dataset available on request from the authors.

Conflicts of Interest: The authors declare no conflicts of interest.

References

1. Hussain, M.K.; Khatoon, S.; Khan, M.F.; Akhtar, M.S.; Ahamad, S.; Saquib, M. Coumarins as Versatile Therapeutic Phytomolecules: A Systematic Review. *Phytomedicine* **2024**, *134*, 155972. [CrossRef]
2. Stefanachi, A.; Leonetti, F.; Pisani, L.; Catto, M.; Carotti, A. Coumarin: A Natural, Privileged and Versatile Scaffold for Bioactive Compounds. *Molecules* **2018**, *23*, 250. [CrossRef]
3. Steinegger, A.; Wolfbeis, O.S.; Borisov, S.M. Optical Sensing and Imaging of pH Values: Spectroscopies, Materials, and Applications. *Chem. Rev.* **2020**, *120*, 12357–12489. [CrossRef]
4. Bureš, F. Fundamental aspects of property tuning in push–pull molecules. *RSC Adv.* **2014**, *4*, 58826–58851. [CrossRef]
5. Udhayakumari, D.; Ramasundaram, S.; Jerome, P.; Oh, T.H. A Review on Small Molecule Based Fluorescence Chemosensors for Bioimaging Applications. *J. Fluoresc.* **2025**, *35*, 3763–3787. [CrossRef] [PubMed]
6. Chen, Y. Recent Advances in Excimer-Based Fluorescence Probes for Biological Applications. *Molecules* **2022**, *27*, 8628. [CrossRef]
7. Wolfbeis, O.S.; Fürlinger, E.; Kroneis, H.; Marsoner, H. A Study on Fluorescent Indicators for Measuring Near-Neutral (“Physiological”) pH Values. *Fresenius J. Anal. Chem.* **1983**, *314*, 119–124. [CrossRef]
8. Wolfbeis, O.S.; Koller, E.; Hochmuth, P. Electronic Spectra and Dissociation Constants of 3-Substituted 7-Hydroxycoumarins. *Bull. Chem. Soc. Jpn.* **1985**, *58*, 731–734. [CrossRef]
9. Molina, P.; Tarraga, A.; Oton, F. Imidazole Derivatives: A Comprehensive Survey of Their Recognition Properties. *Org. Biomol. Chem.* **2012**, *10*, 1711–1724. [CrossRef] [PubMed]
10. Vasylevska, A.S.; Karasyov, A.A.; Borisov, S.M.; Klimant, I. Novel coumarin-based fluorescent pH indicators, probes and membranes covering a broad pH range. *Anal. Bioanal. Chem.* **2007**, *387*, 2131–2141. [CrossRef]
11. Kim, H.; Sarkar, S.; Nandy, M.; Ahn, K.H. Imidazolyl-benzocoumarins as ratiometric fluorescence probes for biologically extreme acidity. *Spectrochim. Acta A Mol. Biomol. Spectrosc.* **2021**, *248*, 119088. [CrossRef]
12. Achelle, S.; Rodríguez-López, J.; Bureš, F.; Robin-le Guen, F. Tuning the Photophysical Properties of Push-Pull Azaheterocyclic Chromophores by Protonation: A Brief Overview of a French-Spanish-Czech Project. *Chem. Rec.* **2020**, *20*, 440–445. [CrossRef]
13. Szwaczko, K.; Kulkowska, A.; Matwijczuk, A. Advances in Coumarin Fluorescent Probes for Medical Diagnostics: A Review of Recent Developments. *Biosensors* **2026**, *16*, 36. [CrossRef]

14. Klikar, M.; Solanke, P.; Tydlitat, J.; Bureš, F. Alphabet-Inspired Design of (Hetero)Aromatic Push-Pull Chromophores. *Chem. Rec.* **2016**, *16*, 1886–1905. [CrossRef]
15. Bhagwat, A.A.; Avhad, K.C.; Patil, D.S.; Nagaiyan, S. Design and Synthesis of Coumarin-Imidazole Hybrid Chromophores: Solvatochromism, Acidochromism and Non-Linear Optical Properties. *Photochem. Photobiol.* **2019**, *95*, 740–754. [CrossRef]
16. Avhad, K.C.; Patil, D.S.; Gawale, Y.K.C.; Sreenath, M.C.S.; Joe, I.H.; Sekar, N. Large Stokes Shifted Far-Red to NIR-Emitting D-π-A Coumarins: Combined Synthesis, Experimental, and Computational Investigation of Spectroscopic and Non-Linear Optical Properties. *ChemistrySelect* **2018**, *3*, 4393–4405. [CrossRef]
17. Boček, I.; Hranjec, M.; Vianello, R. Imidazo [4,5-*b*]pyridine Derived Iminocoumarins as Potential pH Probes: Synthesis, Spectroscopic and Computational Studies of Their Protonation Equilibria. *J. Mol. Liq.* **2022**, *355*, 118982. [CrossRef]
18. Kim, D.; Xuan, Q.P.; Moon, H.; Jun, Y.W.; Ahn, K.H. Synthesis of Benzocoumarins and Characterization of Their Photophysical Properties. *Asian J. Org. Chem.* **2014**, *3*, 1089–1096. [CrossRef]
19. Dai, M.; Sarkar, S.; Song, C.W.; Reo, Y.J.; Yang, Y.J.; Ahn, K.H. Bent-Benzocoumarin Dyes That Fluoresce in Solution and in Solid State and Their Application to Bioimaging. *ChemPhotoChem* **2020**, *4*, 721–728. [CrossRef]
20. Sun, J.; Zheng, M.; Jia, J.; Wang, W.; Cui, Y.; Gao, J. New coumarin-benzoxazole derivatives: Synthesis, photophysical and NLO properties. *Dye. Pigment.* **2019**, *166*, 287–295. [CrossRef]
21. Zhang, G.; Zheng, H.; Liu, G.; Wang, P.; Xiang, R. Synthesis and Application of a Multifunctional Fluorescent Polymer Based on Coumarin. *BioResources* **2016**, *11*, 373–384. [CrossRef]
22. Zhang, G.; Zheng, H.; Guo, M.; Du, L.; Liu, G.; Wang, P. Synthesis of Polymeric Fluorescent Brightener Based on Coumarin and Its Performances on Paper as Light Stabilizer, Fluorescent Brightener and Surface Sizing Agent. *Appl. Surf. Sci.* **2016**, *367*, 167–173. [CrossRef]
23. Wlodarczyk, P.; Komarneni, S.; Roy, R.; White, W.B. Enhanced Fluorescence of Coumarin Laser Dye in the Restricted Geometry of a Porous Nanocomposite. *J. Mater. Chem.* **1996**, *6*, 1967–1969. [CrossRef]
24. Sánchez-de-Armas, R.; San Miguel, M.Á.; Oviedo, J.; Sanz, J.F. Coumarin Derivatives for Dye Sensitized Solar Cells: A TD-DFT Study. *Phys. Chem. Chem. Phys.* **2012**, *14*, 225–233. [CrossRef] [PubMed]
25. Wagner, B.D. The Use of Coumarins as Environmentally-Sensitive Fluorescent Probes of Heterogeneous Inclusion Systems. *Molecules* **2009**, *14*, 210–237. [CrossRef]
26. Xu, H.; Bu, Y.; Wang, J.; Qu, M.; Zhang, J.; Zhu, X.; Liu, G.; Wu, Z.; Chen, G.; Zhou, H. A Convenient Fluorescent Probe for Monitoring Lysosomal pH Change and Imaging Mitophagy in Living Cells. *Sens. Actuators B Chem.* **2021**, *330*, 129333. [CrossRef]
27. Hirano, M.; Kuroda, D.; Watanabe, K.; Miyoshi, N. Application of 2-(3,5,6-trifluoro-2-hydroxy-4-methoxyphenyl)benzoxazole and -benzothiazole to fluorescent probes sensing pH and metal cations. *J. Org. Chem.* **2001**, *66*, 7328–7333. [CrossRef]
28. Beč, A.; Vianello, R.; Hranjec, M. Synthesis and Spectroscopic Characterization of Multifunctional D-π-A Benzimidazole Derivatives as Potential pH Sensors. *J. Mol. Liq.* **2023**, *386*, 122493. [CrossRef]
29. Makowska, A.; Sączewski, F.; Bednarski, P.J.; Gdaniec, M.; Balewski, Ł.; Warmbier, M.; Kornicka, A. Synthesis, Structure and Cytotoxic Properties of Copper(II) Complexes of 2-Iminocoumarins Bearing a 1,3,5-Triazine or Benzoxazole/Benzothiazole Moiety. *Molecules* **2022**, *27*, 7155. [CrossRef]
30. Makowska, A.; Wolff, L.; Sączewski, F.; Bednarski, P.J.; Kornicka, A. Synthesis and Cytotoxic Evaluation of Benzoxazole/Benzothiazole-2-Imino-Coumarin Hybrids and Their Coumarin Analogues as Potential Anticancer Agents. *Pharmazie* **2019**, *74*, 648–657. [CrossRef]
31. Ben Ammar, H.; Kaddachi, M.T.; Kahn, P.H. Conversion of Malononitrile into 2-Cyanomethyl Compounds. *Phys. Chem. News* **2003**, *9*, 137–139.
32. Perin, N.; Cindrić, M.; Vervaeke, P.; Liekens, S.; Mašek, T.; Starčević, K.; Hranjec, M. Benzazole Substituted Iminocoumarins as Potential Antioxidants with Antiproliferative Activity. *Med. Chem.* **2021**, *17*, 13–20. [CrossRef]
33. Bursch, M.; Krossing, I.; Grimme, S. Best-Practice DFT Protocols for Basic Molecular Computational Chemistry. *Angew. Chem. Int. Ed.* **2022**, *61*, e202205735. [CrossRef]
34. Tandarić, T.; Vianello, R. Computational Insight into the Mechanism of the Irreversible Inhibition of Monoamine Oxidase Enzymes by the Antiparkinsonian Propargylamine Inhibitors Rasagiline and Selegiline. *ACS Chem. Neurosci.* **2019**, *10*, 3532–3542. [CrossRef]
35. Tissandier, M.D.; Cowen, K.A.; Feng, W.Y.; Gundlach, E.; Cohen, M.H.; Earhart, A.D.; Coe, J.V.; Tuttle, T.R. The Proton's Absolute Aqueous Enthalpy and Gibbs Free Energy of Solvation from Cluster-Ion Solvation Data. *J. Phys. Chem. A* **1998**, *102*, 7787–7794. [CrossRef]
36. Marenich, A.V.; Cramer, C.J.; Truhlar, D.G. Universal Solvation Model Based on Solute Electron Density and on a Continuum Model of the Solvent Defined by the Bulk Dielectric Constant and Atomic Surface Tensions. *J. Phys. Chem. B* **2009**, *113*, 6378–6396. [CrossRef]
37. Frisch, M.J.; Trucks, G.W.; Schlegel, H.B.; Scuseria, G.E.; Robb, M.A.; Cheeseman, J.R.; Scalmani, G.; Barone, V.; Petersson, G.A.; Nakatsuji, H.; et al. *Gaussian 16, Revision C.01*; Gaussian, Inc.: Wallingford, CT, USA, 2016.

38. Rastija, V.; Vrandečić, K.; Ćosić, J.; Majić, I.; Kanižai Šarić, G.; Agić, D.; Karnaš, M.; Lončarić, M.; Molnar, M. Biological Activities Related to Plant Protection and Environmental Effects of Coumarin Derivatives: QSAR and Molecular Docking Studies. *Int. J. Mol. Sci.* **2021**, *22*, 7283. [CrossRef] [PubMed]
39. Kristinsson, H. Synthese von Heterocyclen; IV1. Neuer Syntheseweg zur Herstellung von Heterocyclischen Nitrilen. *Synthesis* **1979**, *1979*, 102–103. [CrossRef]
40. Sakamoto, M.; Nozaka, P.A.; Shimamoto, M.; Ozaki, H.; Suzuki, Y.; Yoshioka, S.; Nagano, M.; Okamura, K.; Dateb, T.; Tamura, O. Synthesis of 2-Substituted Benzoxazoles. *J. Chem. Soc. Perkin Trans. 1* **1995**, *13*, 1759–1770. [CrossRef]
41. Liu, H.; Chen, L.; Zhou, F.; Zhang, Y.-X.; Xu, J.; Xu, M.; Bai, S.-P. Anti-Oligomerization Sheet Molecules: Design, Synthesis and Evaluation of Inhibitory Activities against α-Synuclein Aggregation. *Bioorg. Med. Chem.* **2019**, *27*, 3089–3096. [CrossRef] [PubMed]
42. Luo, F.T.; Jeevanandam, A. Simple Transformation of Nitrile into Ester by the Use of Chlorotrimethylsilane. *Tetrahedron Lett.* **1998**, *39*, 9455–9456. [CrossRef]
43. Kiyani, H.; Daroonkala, M.D. A Cost-Effective and Green Aqueous Synthesis of 3-Substituted Coumarins Catalyzed by Potassium Phthalimide. *Bull. Chem. Soc. Ethiop.* **2015**, *29*, 449–456. [CrossRef]
44. Reichardt, C.; Welton, T. *Solvents and Solvent Effects in Organic Chemistry*, 4th ed.; Wiley-VCH: Weinheim, Germany, 2011. [CrossRef]
45. Gonjo, T.; Futami, Y.; Morisawa, Y.; Wojcik, M.J.; Ozaki, Y. Hydrogen Bonding Effects on the Wavenumbers and Absorption Intensities of the OH Fundamental and the First, Second, and Third Overtones of Phenol and 2,6-Dihalogenated Phenols Studied by Visible/Near-Infrared/Infrared Spectroscopy. *J. Phys. Chem. A* **2011**, *115*, 9845–9853. [CrossRef]
46. Li, D.; Li, C.; Liu, Y. Effects of Solvent Polarity and Hydrogen Bonding on Coumarin 500. *J. Mol. Liq.* **2016**, *218*, 670–675. [CrossRef]
47. Wang, B.; Anslyn, E.V. *Chemosensors: Principles, Strategies and Applications*; Wiley-VCH: Weinheim, Germany, 2011. [CrossRef]
48. Demchenko, A.P. *Introduction to Fluorescence Sensing*; Springer: Cham, Switzerland, 2015. [CrossRef]
49. Tshepelevitsh, S.; Kütt, A.; Lõkov, M.; Kaljurand, I.; Saame, J.; Heering, A.; Plieger, P.; Vianello, R.; Leito, I. On the Basicity of Organic Bases in Different Media. *Eur. J. Org. Chem.* **2019**, *2019*, 6735–6748. [CrossRef]
50. Lõkov, M.; Tshepelevitsh, S.; Heering, A.; Plieger, P.G.; Vianello, R.; Leito, I. On the Basicity of Conjugated Nitrogen Heterocycles in Different Media. *Eur. J. Org. Chem.* **2017**, *2017*, 4475–4489. [CrossRef]
51. Wang, F.; Yang, Z.; Yan, J.; Xue, Q. Direct Arylation of Benzoxazoles with Benzoyl Chlorides under Mild Conditions. *Eur. J. Org. Chem.* **2024**, *27*, e202400303. [CrossRef]
52. Benassi, R.; Grandi, R.; Pagnoni, U.M.; Taddei, F. Study of the Effect of N-Protonation and N-Methylation on the 1H and 13C Chemical Shifts of the Six-Membered Ring in Benzazoles and 2-Substituted N,N-Dimethylamino Derivatives. *Magn. Reson. Chem.* **1986**, *24*, 415–420. [CrossRef]
53. Jackson, P.F.; Morgan, K.J.; Turner, A.M. Studies in Heterocyclic Chemistry. Part IV. Kinetics and Mechanisms for the Hydrolysis of Benzoxazoles. *J. Chem. Soc. Perkin Trans. 2* **1972**, 1582–1587. [CrossRef]
54. Holmes, G.A.; Rice, K.; Snyder, C.R. Ballistic Fibers: A Review of the Thermal, Ultraviolet and Hydrolytic Stability of the Benzoxazole Ring Structure. *J. Mater. Sci.* **2006**, *41*, 4105–4116. [CrossRef]
55. Scherm, B.; Balmas, V.; Spanu, F.; Pani, G.; Delogu, G.; Pasquali, M.; Migheli, Q. The Wheat Pathogen *Fusarium culmorum*. *Mol. Plant Pathol.* **2013**, *14*, 323–341. [CrossRef]
56. Bolton, M.D.; Thomma, B.P.; Nelson, B.D. *Sclerotinia sclerotiorum* (Lib.) de Bary: Biology and Molecular Traits of a Cosmopolitan Pathogen. *Mol. Plant Pathol.* **2006**, *7*, 1–16. [CrossRef]
57. Marquez, N.; Giachero, M.L.; Declerck, S.; Ducasse, D.A. *Macrophomina phaseolina*: General Characteristics of Pathogenicity and Methods of Control. *Front. Plant Sci.* **2021**, *12*, 634397. [CrossRef] [PubMed]
58. Abdel-Aziem, A.; Baaiu, B.S.; Abdelhamid, A.O. Synthesis and Evaluation of Antimicrobial Activity of Some Novel Heterocyclic Compounds from 5-Bromosalicylaldehyde. *J. Heterocycl. Chem.* **2017**, *54*, 3471–3480. [CrossRef]
59. Wei, Y.; Peng, W.; Wang, D.; Hao, S.-H.; Li, W.-W.; Ding, F. Design, Synthesis, Antifungal Activity, and 3D-QSAR of Coumarin Derivatives. *J. Pestic. Sci.* **2018**, *43*, 88–95. [CrossRef] [PubMed]
60. de Araújo, R.S.; Guerra, F.Q.; de O. Lima, E.; De Simone, C.A.; Tavares, J.F.; Scotti, L.; Scotti, M.T.; De Aquino, T.M.; De Moura, R.O.; Mendonça, F.J.B.; et al. Synthesis, Structure-Activity Relationships (SAR) and In Silico Studies of Coumarin Derivatives with Antifungal Activity. *Int. J. Mol. Sci.* **2013**, *14*, 1293–1309. [CrossRef]

61. Kakkar, S.; Tahlan, S.; Lim, S.M.; Ramasamy, K.; Mani, V.; Shah, S.A.A.; Narasimhan, B. Benzoxazole derivatives: Design, synthesis and biological evaluation. *Chem. Cent. J.* **2018**, *12*, 92. [CrossRef] [PubMed]
62. Fuentes-Aguilar, A.; Merino-Montiel, P.; Montiel-Smith, S.; Meza-Reyes, S.; Vega-Báez, J.L.; Puerta, A.; Fernandes, M.X.; Padrón, J.M.; Petreni, A.; Nocentini, A.; et al. 2-Aminobenzoxazole-appended coumarins as potent and selective inhibitors of tumour-associated carbonic anhydrases. *J. Enzyme Inhib. Med. Chem.* **2022**, *37*, 168–177. [CrossRef]